

Hidden magnetism uncovered in charge ordered bilayer kagome material ScV_6Sn_6

Z. Guguchia,^{1,*} D.J. Gawryluk,^{2,†} Soohyeon Shin,^{2,‡} Z. Hao,^{3,‡} C. Mielke III,^{1,4} D. Das,¹ I. Plokhikh,² L. Liborio,⁵ K. Shenton,⁵ Y. Hu,⁶ V. Sazgari,¹ M. Medarde,⁷ H. Deng,³ Y. Cai,⁸ C. Chen,⁸ Y. Jiang,⁹ A. Amato,¹ M. Shi,⁶ M.Z. Hasan,^{9,10,11} J.-X. Yin,³ R. Khasanov,¹ E. Pomjakushina,² and H. Luetkens¹

¹Laboratory for Muon Spin Spectroscopy, Paul Scherrer Institute, CH-5232 Villigen PSI, Switzerland

²Laboratory for Multiscale Materials Experiments,

Paul Scherrer Institut, 5232, Villigen PSI, Switzerland

³Department of Physics, Southern University of Science and Technology, Shenzhen, Guangdong, 518055, China

⁴Physik-Institut, Universität Zürich, Winterthurerstrasse 190, CH-8057 Zürich, Switzerland

⁵Scientific Computing Department, Science & Technology Facilities Council, Rutherford Appleton Laboratory, Didcot OX11 0QX, United Kingdom

⁶Photon Science Division, Paul Scherrer Institut, CH-5232 Villigen PSI, Switzerland

⁷Laboratory for Multiscale Materials Experiments,

Paul Scherrer Institut, CH-5232 Villigen PSI, Switzerland

⁸Shenzhen Institute for Quantum Science and Engineering,

Southern University of Science and Technology, Shenzhen 518055, China

⁹Laboratory for Topological Quantum Matter and Advanced Spectroscopy (B7), Department of Physics, Princeton University, Princeton, New Jersey 08544, USA

¹⁰Princeton Institute for the Science and Technology of Materials,

Princeton University, Princeton, New Jersey 08540, USA

¹¹Quantum Science Center, Oak Ridge, Tennessee 37831, USA

Charge ordered kagome lattices have been demonstrated to be intriguing platforms for studying the intertwining of topology, correlation, and magnetism. The recently discovered charge ordered kagome material ScV_6Sn_6 does not feature a magnetic groundstate or excitations, thus it is often regarded as a conventional paramagnet. Here, using advanced muon-spin rotation spectroscopy, we uncover an unexpected hidden magnetism of the charge order. We observe a striking enhancement of the internal field width sensed by the muon ensemble, which takes place within the charge ordered state. More remarkably, the muon spin relaxation rate below the charge ordering temperature is substantially enhanced by applying an external magnetic field. Taken together with the hidden magnetism found in AV_3Sb_5 ($A = \text{K}, \text{Rb}, \text{Cs}$) and FeGe kagome systems, our results suggest ubiquitous time-reversal symmetry-breaking in charge ordered kagome lattices.

One of the most scientifically fruitful families of layered systems shown to host intriguing and exotic physics are the kagome lattice materials^{1–5}, composed of a two-dimensional lattice of corner-sharing triangles. This unique geometry gives rise to frustration, correlated quantum orders, and topology, owing to its special features: the electronic structure hosts a flat band, inflection points called “van Hove singularities“, and Dirac cones.

The recently discovered AV_3Sb_5 ($A = \text{K}, \text{Rb}, \text{Cs}$)^{6–8} family of materials, crystallizing in a structurally perfect two-dimensional kagome net of vanadium atoms, shows the typical kagome band structure and exhibits two correlated orders: high-temperature charge order and a superconducting instability at lower temperatures^{9–11}. The unique feature of AV_3Sb_5 is the emergence of a time-

reversal symmetry breaking chiral charge order with both magnetic^{12–16,18–20,31} and electronic anomalies^{21,22}. Theoretically, these features could be explained by a complex order parameter realizing a higher angular momentum state, dubbed unconventional, in analogy to superconducting orders^{23–28}.

RV_6Sn_6 ($R = \text{Sc}, \text{Y}$, or rare earth)^{29–32} is a more recent family of kagome metals that has a similar vanadium structural motif as the AV_3Sb_5 ($A = \text{K}, \text{Rb}, \text{Cs}$) compounds. However, ScV_6Sn_6 is the only compound among the series of RV_6Sn_6 that has been found to host charge order below $T^* \simeq 90 \text{ K}$ ³². Some distinct characteristics^{33–36} of charge order such as different propagation vectors and distinct electron-phonon coupling strength³⁵ have been reported in these two families of kagome metals. However, ScV_6Sn_6 shows no superconductivity even after suppression of charge order by hydrostatic pressure³⁷. One of the most intriguing questions about the charge order in ScV_6Sn_6 is whether or not it breaks time-reversal symmetry.

In this paper, we utilize the combination of zero-field (ZF) and transverse-field (TF) μSR techniques to probe the μSR relaxation rates in ScV_6Sn_6 as a function of temperature and magnetic field. We detect an enhancement of the muon-spin depolarization rate below the charge order temperature T^* . The rate is further and significantly enhanced by applying an external magnetic field along the crystallographic c -axis, which is indicative of a strong contribution of electronic origin to the muon spin relaxation below the charge ordering temperature. These results point to a complex electronic response strongly intertwined with the charge order in the kagome system ScV_6Sn_6 and provide useful insights into the microscopic mechanisms involved in the charge density wave order.

The layered crystal structure of ScV_6Sn_6 with its V

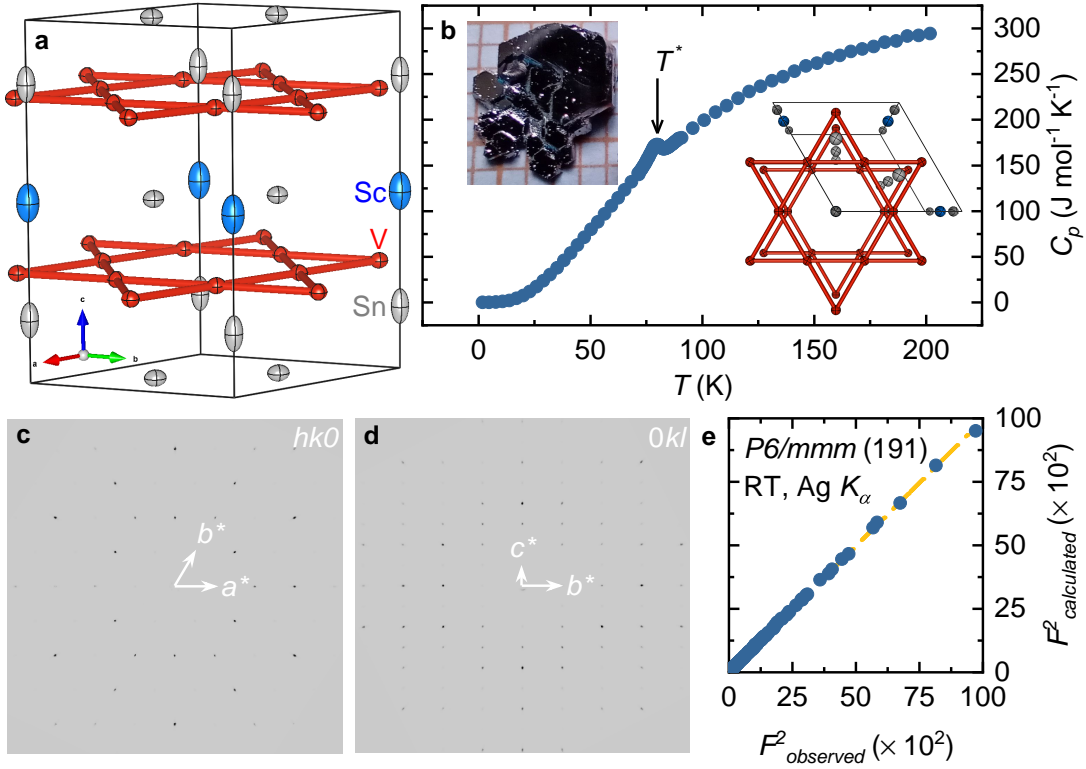


Figure 1: **Crystal structure of ScV_6Sn_6 .** **a**, Room temperature (RT) crystal structures of ScV_6Sn_6 with atomic displacement ellipsoids as determined from laboratory single-crystal X-ray diffraction ($\text{Ag } K_\alpha$) using the Space Group (SG) $P6/mmm$ (191) highlighting the kagome lattice pattern of the vanadium atoms. **b**, Temperature dependence of the heat capacity for the ScV_6Sn_6 single crystals. Insets show a photograph of ScV_6Sn_6 single crystal and the crystal structure along c -direction. **c**, and **d**, Reciprocal ($hk0$) and ($0kl$) respectively, lattice planes measured by laboratory X-ray diffraction at RT for a ScV_6Sn_6 single crystal, illustrating the agreement between the observed systematic absences and those of the $P6/mmm$ SG. **e**, Agreement between the observed and calculated diffraction data at RT, as obtained from structural refinements using the *Olexs*² software³⁸ with *ShelXL* package³⁹. Structures were plotted using the *VESTA* visualization tool⁴⁰.

atoms arranged in a kagome network is shown in Figure 1a. Figure 1b presents the temperature dependence of the specific heat capacity, C_p . A well pronounced peak in the heat capacity, corresponding to the charge order transition at $T^* \simeq 80$ K, is clearly seen, which provides evidence of a bulk phase transition. Single crystal X-ray diffraction measurements (see Fig. 1c-e) confirm that the as-grown sample is a high-quality single crystal in the space group $P6/mmm$. The lattice parameters $a = 5.4739(3)$ Å and $c = 9.1988(7)$ Å at room temperature are close those reported in previous studies³².

Magnetotransport data provide further evidence for the charge order transition. Magnetotransport has been shown to be particularly sensitive for detecting the CDW transition, since the magnetoresistance (MR) is a measure of the mean free path integrated over the Fermi surface and can detect a change of the scattering anisotropy and/or a Fermi surface reconstruction reliably. The MR under perpendicular magnetic field in ScV_6Sn_6 from 1.9 K to 120 K is shown in Fig. 2a. At high temperatures, MR adopts a standard quadratic dependence with $\mu_0 H$ ($\mu_0 H$ is the applied magnetic field) and can be well fitted to a polynomial: $\Delta\rho/\rho_{H=0} = \alpha + \beta \cdot H^n$ (where α ,

β and n are fitting parameters) with n close to 2. MR shows deviation from quadratic field dependence upon lowering the temperature and becomes nearly linear deep within the charge-ordered state. The exponent is estimated to be $n \simeq 1.2$ at 1.9 K. Linear MR has usually been considered as a hallmark feature of an unconventional quantum state as such behaviour was previously observed in unconventional superconductors⁴¹, topological⁴² and charge/spin density wave materials^{21,43}. For further insight, we provide the so called Kohler plot, $\Delta\rho/\rho_{H=0}$ vs $(\mu_0 H/\rho_{H=0})^2$, which is shown in Fig. 2b. The most striking feature of this plot is that the MR data collapse to one line for all temperatures below $T^* \simeq 80$ K while they show a pronounced T -dependence above T^* . This effect may arise from a Fermi surface reconstruction caused by the CDW order.

Our scanning tunneling microscopy (STM) experiments provide direct confirmation for the charge order with an in-plane unit cell enlargement of $\sqrt{3} \times \sqrt{3}$ (see Fig. 2c). The angle-resolved photoemission spectroscopy (ARPES) shows that the Fermi surface has stronger intensities at K and K' points (see Fig. 2d and also Ref.³⁵). The autocorrelation of such Fermi surface data is consis-

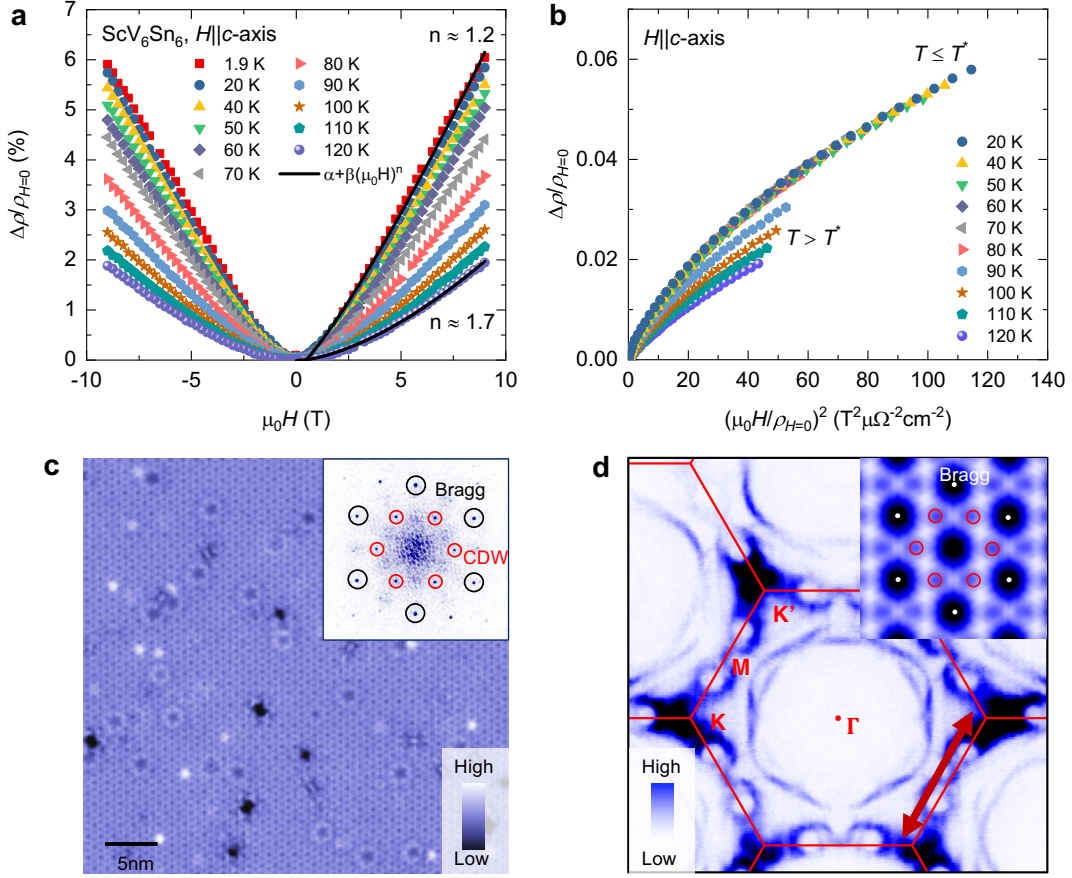


Figure 2: **Magnetotransport characteristics and charge density wave with an in-plane unit cell enlargement of $\sqrt{3} \times \sqrt{3}$ for ScV_6Sn_6 .** **a**, The magnetoresistance measured at various temperatures above and below the charge ordering temperature $T^* \simeq 80$ K. Black solid lines represent fits to the data by means of the following equation: $\Delta\rho/\rho_{H=0} = \alpha + \beta \cdot H^n$. **b**, Kohler plot, $\Delta\rho/\rho_{H=0}$ vs $(\mu_0 H/\rho_{H=0})^2$, of the magnetoresistance, plotted from field-sweeps at various temperatures. **c**, STM dI/dV spectroscopic map and corresponding Fourier transform (inset). The red circled marks the $\sqrt{3} \times \sqrt{3}$ CDW. Data taken at $V = 100$ meV, $I = 0.5$ nA, $T = 4.5$ K, $V_{\text{mod}} = 10$ meV. **d**, Fermi surface obtained by ARPES showing stronger intensities near K points. The inset shows the autocorrelation of the Fermi surface, highlighting the instability with a vector of $\sqrt{3} \times \sqrt{3}$ as marked by the red circles. This vector corresponds to the scattering between states at K and K' points as marked by the arrow in the main figure. Data taken at 10 K.

tent with instabilities at vectors featuring a $\sqrt{3} \times \sqrt{3}$ unit cell enlargement.

Next, in order to search for any magnetism (static or slowly fluctuating) associated with charge order in ScV_6Sn_6 , zero-field μSR experiments have been carried out above and below the charge order temperature T^* . A schematic overview of the experimental setup with the muon spin forming 45° with respect to the c -axis of the crystal is shown in Figure 3a. The sample was surrounded by four detectors: Forward (1), Backward (2), Up (3), and Down (4). Figure 3b displays the zero-field μSR spectra from detectors 3 & 4 collected over a wide temperature range. The ZF- μSR spectrum is characterised by a weak depolarization of the muon spin ensemble and show no evidence of long-range ordered magnetism in ScV_6Sn_6 . However, it shows that the muon spin relaxation has a clearly observable temperature de-

pendence. Figure 3c displays the μSR spectra collected at 5 K in zero-field and at various external magnetic fields applied longitudinal to the muon spin polarization, $B_{\text{LF}} \simeq 1\text{-}25$ mT. Since the full polarization can be recovered by the application of a small external longitudinal magnetic field, $B_{\text{LF}} = 5$ mT, the relaxation is, therefore, due to spontaneous fields which are static on the microsecond timescale⁴⁹. Similar to AV_3Sb_5 , the zero-field μSR spectra for ScV_6Sn_6 were fitted using the gaussian Kubo-Toyabe depolarization function⁴⁴, multiplied by an additional exponential $\exp(-\Gamma t)$ term

$$P_{ZF}^{GKT}(t) = \left(\frac{1}{3} + \frac{2}{3}(1 - \Delta^2 t^2) \exp\left[-\frac{\Delta^2 t^2}{2}\right] \right) \exp(-\Gamma t) \quad (1)$$

where Δ/γ_μ is the width of the local field distribution primarily due to the nuclear moments. However, this

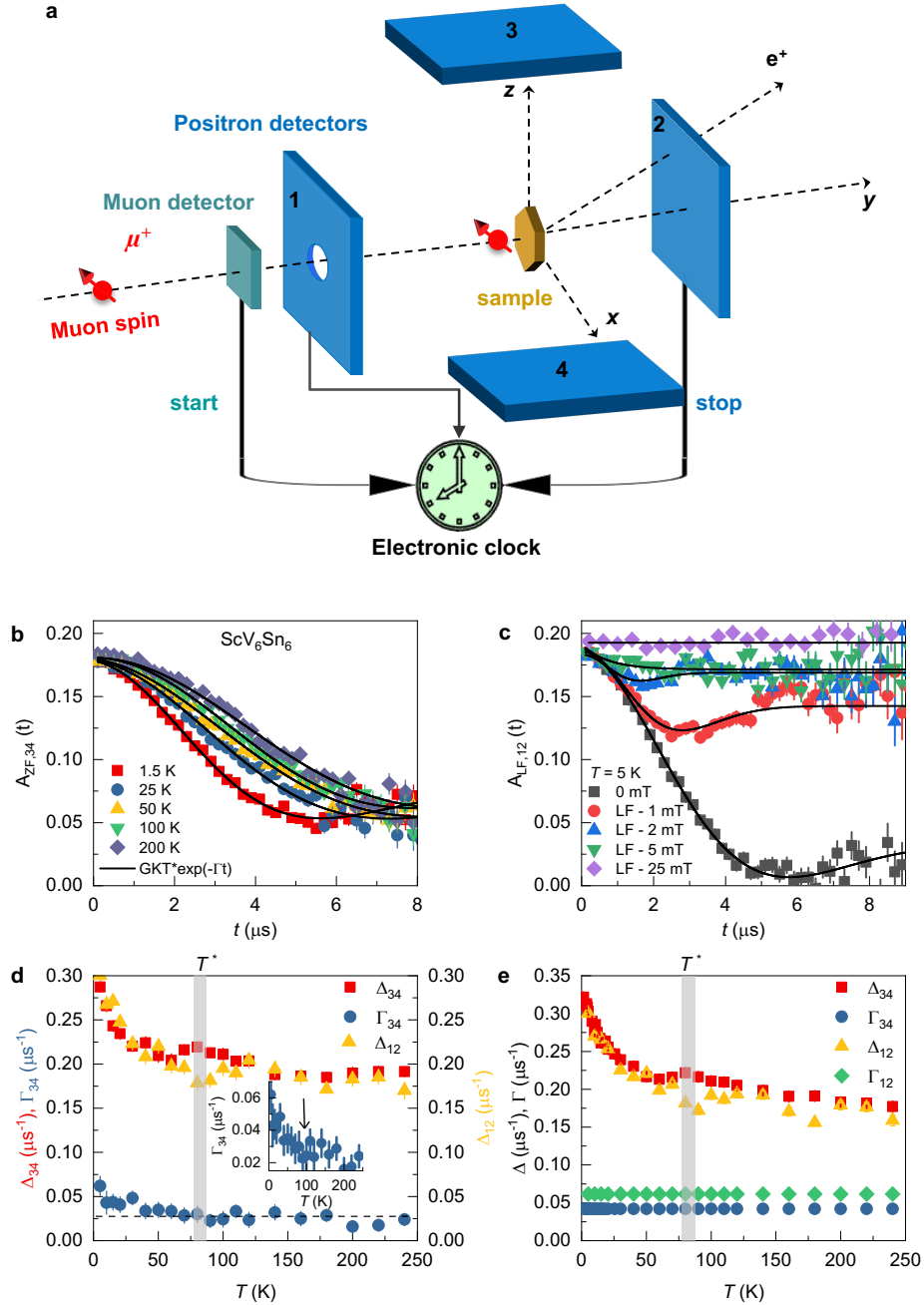


Figure 3: **Magnetic response of the charge order in ScV_6Sn_6 .** **a**, Overview of the experimental setup. Spin polarized muons with spin S_μ , forming 45° with respect to the c -axis of the crystal, are implanted in the sample, which is surrounded by four positron detectors: Forward (1), Backward (2), Up (3), and Down (4). A clock is started at the time the muon surpasses the muon detector (M) and is stopped as soon as the decay positron is detected in one of the detectors. **b**, The ZF μ SR time spectra for ScV_6Sn_6 , obtained at different temperatures. The solid black curves in panel **b** represent fits to the recorded time spectra, using the Eq. 1. Error bars are the standard error of the mean (s.e.m.) in about 10^6 events. **c**, The μ SR time spectra for ScV_6Sn_6 , obtained at $T = 5$ K in zero-field and at various external magnetic field applied longitudinal to the muon spin polarization. The solid black curves in panel **c** represent fits to the recorded time spectra, using the Eq. 1. Error bars are the standard error of the mean (s.e.m.) in about 10^6 events. **d** – **e**, The temperature dependences of the relaxation rates Δ and Γ from two sets of detectors, obtained in a wide temperature range across the charge ordering temperature $T^* \simeq 80$ K. In panel **e** the rate Γ is kept constant as a function of temperature. The error bars represent the standard deviation of the fit parameters.

Gaussian component may also include the field distribution at the muon site created by a dense network of weak

electronic moments. $\gamma_\mu/2\pi = 135.5$ MHz/T is the muon gyromagnetic ratio. The exponential term Γ may e.g. be due to the presence of electric field gradients, causing deviations from the GKT-like spectrum or dilute electronic moments. Δ_{34} shows a non-monotonous temperature dependence; namely, a peak coinciding with the onset of the charge order, which decreases to a broad minimum before increasing again towards lower temperatures. Δ_{12} instead shows a weak minimum at T^* with the significant increase at lower temperatures. The onset of charge order might alter the electric field gradient experienced by the nuclei, due to the fact that the quantization axis for the nuclear moments depends on the electric field gradients (EFG), and correspondingly the magnetic dipolar coupling of the muon to the nuclei⁴⁵. This can induce a change in the nuclear dipole contribution to the zero-field μ SR signal and may explain the small maximum or minimum in Δ_{34} and Δ_{12} , respectively, at the onset of T^* . However, the significant increase of both Δ_{34} and Δ_{12} at lower temperatures is difficult to explain with the change of the EFG and suggests a considerable contribution of electronic origin (dense moments) to the muon spin relaxation in the charge ordered state. There is also a noteworthy increase in the relaxation rate Γ_{34} upon lowering the temperature below the charge ordering temperature T^* , which is better visible in the inset of Fig. 3d. Moreover, our high field μ SR results presented below definitively prove that there is indeed a strong contribution of electronic origin to the muon spin relaxation below the charge ordering temperature (see below). In sum, the ZF- μ SR results indicate that there is an enhanced width of internal fields sensed by the muon ensemble below $T^* \simeq 80$ K. The increase of Δ and Γ below T^* as well as the dip-like feature around T^* are reminiscent of the behavior observed in other kagome systems AV_3Sb_5 ($A = K, Rb, Cs$). The increase in Δ_{34} and Δ_{12} below T^* in ScV_6Sn_6 is estimated to be $\simeq 0.1 \mu s^{-1}$ and $\simeq 0.12 \mu s^{-1}$, respectively, which can be interpreted as a characteristic field strength $\Delta_{34,12}/\gamma_\mu \simeq 1.2-1.5$ G. We note that this value is by factor of $\sim 4-5$ higher than the one reported previously for AV_3Sb_5 ($A = K, Rb, Cs$). A similar increase of internal magnetic field strength is reported in several time-reversal symmetry-breaking superconductors⁴⁶ and in some multigap TRS breaking superconductors (e.g. La_7Ni_3 ⁴⁷) across T_c .

In order to substantiate the zero-field μ SR results, presented above, we carried out systematic high field μ SR⁴⁸ experiments. Under high magnetic field, the direction of the applied field defines the quantization axis for the nuclear moments, so that the effect of the charge order on the electric field gradient at the nuclear sites is irrelevant. For the high-field experiments, a mosaic of several crystals was used. The individual crystals were glued to a 10 mm circular silver sample holder and the entire ensemble was held together by small droplets of GE varnish. Figure 4a shows the probability field distribution, measured at 3 K in a magnetic field of 8 T applied along the crystallographic c -axis. In the whole investigated tem-

perature range, two-component signals were observed: a signal with fast relaxation $\sigma_{TF} \simeq 0.428(3) \mu s^{-1}$ (broad signal on the left side of the Fourier spectrum) and another one with a slow relaxation $0.05 \mu s^{-1}$ (narrow signal). The narrow signal arises mostly from the muons stopping in the silver sample holder and its position is a precise measure of the value of the applied magnetic field. The width and the position of the narrow signal is found to be temperature independent, as expected, and thus were kept constant in the analysis. The relative fraction of the muons stopping in the sample was fixed to the value obtained at the base- T and kept temperature independent. The signal with the fast relaxation, which is shifted towards a lower field from the applied one, arises from the muons stopping in the sample and it takes a major fraction (~ 50 %) of the μ SR signal. This points to the fact that the sample response arises from the bulk of the sample. A non-monotonous behaviour of the relaxation rate is clearly seen in the μ SR data, measured in magnetic field of 0.01 T, applied parallel to the c -axis, as shown in Fig. 4b. This looks similar to the temperature dependence of the zero-field rate Δ_{34} . At higher fields such as 2 T, 4 T, 6 T, and 8 T, the rate shows a clear and stronger increase towards low temperatures within the charge ordered state. As the nuclear contribution to the relaxation cannot be enhanced by an external field, this indicates that the low-temperature relaxation rate in magnetic fields is dominated by the electronic contribution. Remarkably, we find that the absolute increase of the relaxation rate between the onset of charge order T^* and the base- T in 8 T is $\Delta\sigma_{TF} \simeq 0.23 \mu s^{-1}$ which is a factor of two higher than the one $0.12 \mu s^{-1}$ observed in zero-field. The transverse-field relaxation is normally smaller by a factor of ~ 2 than expected from the zero-field measurements⁴⁹. This is because in transverse-field measurements only the width in one direction is relevant while in ZF the width in two directions is relevant. This means that the relaxation for ScV_6Sn_6 in high transverse-field is actually a factor of four higher than in ZF. This indicates a strong field-induced enhancement of the electronic response. We also note that a weak but non-negligible field effect on the relaxation rate is observed above T^* within a 20-30 K temperature range, which may point towards the charge density wave fluctuations preceding the phase transition.

Based on the unique combination of ZF- μ SR and high-field μ SR experiments, we observed a magnetic response (enhanced internal field width) below $T^* \simeq 80$ K, providing direct evidence for the time-reversal symmetry-breaking fields in the kagome lattice of ScV_6Sn_6 . Since at least 50 % of the sample volume experiences an increase in the relaxation rate, this indicates the bulk nature of the transition below T^* . The presence of an electronic response and its field induced enhancement in ScV_6Sn_6 is similar to our previous observations in kagome lattice superconductors AV_3Sb_5 ($A = K, Rb, Cs$)¹²⁻¹⁴.

We specify some similarities and differences between ScV_6Sn_6 and AV_3Sb_5 : (1) In ScV_6Sn_6 , we observed the

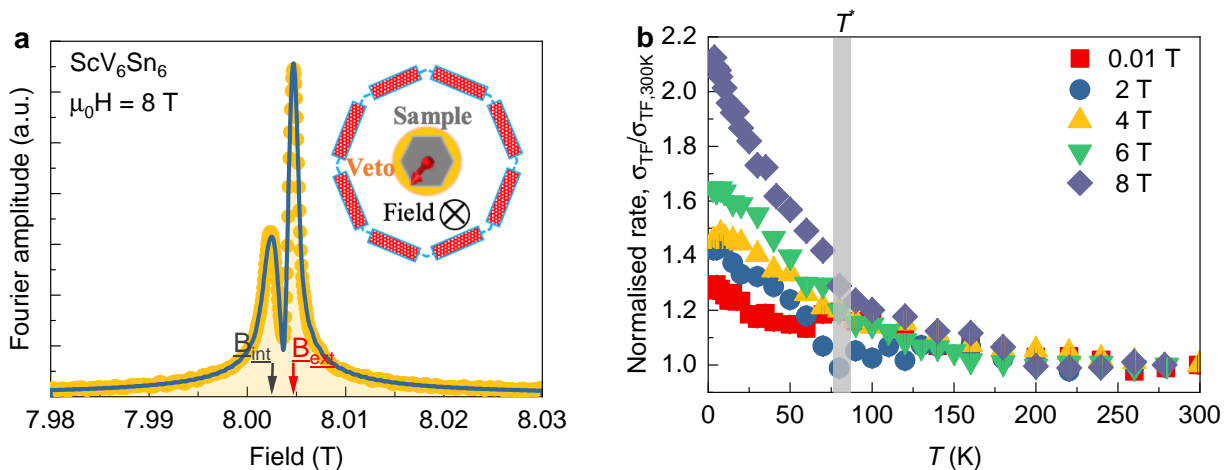


Figure 4: **Enhanced magnetic response of the charge order with applying external magnetic fields.** **a**, Fourier transform of the μ SR asymmetry spectra for a mosaic of single crystals of ScV_6Sn_6 at 3 K in the presence of an applied field of $\mu_0 H = 8$ T. The black solid line is a two-component signal fit. The peaks marked by the arrows denote the external and internal fields, determined as the mean values of the field distribution from the silver sample holder and from the sample, respectively. Inset shows the schematic high-field μ SR experimental setup. The sample was surrounded by 2×8 positron detectors, arranged in rings. The specimen was mounted in a He gas-flow cryostat with the largest face perpendicular to the muon beam direction, along which the external field was applied. Behind the sample lies a veto counter (in orange) which rejects the muons that do not hit the sample. **b**, Temperature dependence of the high transverse field muon spin relaxation rate σ_{TF} for the single crystal of ScV_6Sn_6 , normalized to the value at 300 K, measured under different c -axis magnetic fields. The vertical grey lines mark the charge ordering temperature, determined from specific heat measurements. The error bars represent the standard deviation of the fit parameters.

enhancement of the rate Γ_{34} by $0.03 \mu\text{s}^{-1}$ below T^* , which is similar to KV_3Sb_5 . On the other hand, the Gaussian rate Δ_{34} and Δ_{12} show significant increase, i.e. by $0.12 \mu\text{s}^{-1}$, in ScV_6Sn_6 , while it shows only a very weak temperature dependence at low temperatures in AV_3Sb_5 . These results show that the increase of relaxation in ScV_6Sn_6 is due predominantly to Gaussian rate. This indicates that internal fields arise from a network of dense weak electronic moments in ScV_6Sn_6 , while the electronic moments seem to be more dilute or more dynamic in AV_3Sb_5 . (2) Among the three compounds AV_3Sb_5 ($A = \text{K}, \text{Rb}, \text{Cs}$) the largest increase of the zero-field relaxation rate below T^* was observed for RbV_3Sb_5 . In ScV_6Sn_6 , the increase of the zero-field relaxation is $0.12 \mu\text{s}^{-1}$, which is a factor of two higher than the one $0.06 \mu\text{s}^{-1}$ observed in RbV_3Sb_5 . (3) The largest field effect was observed in KV_3Sb_5 . In ScV_6Sn_6 , magnetic field also leads to the enhancement of the rate and the increase of the rate reaches a value of $0.23 \mu\text{s}^{-1}$ at 8 T. This is a factor of 1.6 higher than the one ($0.15 \mu\text{s}^{-1}$) observed in KV_3Sb_5 . The AV_3Sb_5 systems are close to the condition of a kagome lattice with van Hove filling and with extended Coulomb interactions^{12,23}. TRS breaking charge order in AV_3Sb_5 was interpreted in terms of orbital current order^{23–28}, which may fundamentally affect the superconducting state. Muons couple to the closed current orbits below T^* , leading to an enhanced internal field width sensed by the muon ensemble concurrent with the charge order^{12,13}. So far, no theoretical proposal for the orbital current order was reported for ScV_6Sn_6 .

In addition, recent STM and ARPES results^{34,36} reveal that the nature of the CDW order in ScV_6Sn_6 is different from AV_3Sb_5 . With the lack of theoretical understanding of ScV_6Sn_6 , we cannot conclude on the origin of the TRS breaking field in this system. But, our results provide key evidence that the magnetic and charge channels of ScV_6Sn_6 are strongly intertwined and will inspire future experiments, particularly neutron scattering with polarization analysis, to potentially understand the precise origin of the observed magnetism.

The exploration of unconventional electronic phases that result from strong electronic correlations is a frontier in condensed matter physics. Kagome lattice systems appear to be an ideal setting in which strongly correlated topological electronic states may emerge. Most recently, the kagome lattice of AV_3Sb_5 has shown to host unconventional chiral charge order, which is analogous to the long-sought-after quantum order in the Haldane model⁵⁰ for honeycomb lattice or Varma model⁵¹ for cuprate high-temperature superconductors. Here we employ muon spin relaxation to probe the magnetic response of kagome charge order on a microscopic level in newly discovered ScV_6Sn_6 with a vanadium kagome lattice. We found an enhancement of the internal field width sensed by the muon ensemble, which takes place within the charge ordered state. The muon spin relaxation rate below the charge ordering temperature is substantially enhanced by applying an external magnetic field. Our work points to a time-reversal symmetry-breaking charge order in ScV_6Sn_6 and extends the classification of mate-

rials with unconventional charge order beyond the series of compounds AV_3Sb_5 ($A = K, Rb, Cs$).

- * Electronic address: zurab.guguchia@psi.ch
 † Electronic address: dariusz.gawryluk@psi.ch
 ‡ These authors contributed equally to the paper.
- ¹ Syôzi, I. Statistics of Kagome Lattice. *Prog. Theor. Phys.* **6**, 306 (1951).
 - ² Zhou, Y., Kanoda, K., & Ng, T.-K. Quantum spin liquid states. *Rev. Mod. Phys.* **89**, 025003 (2017).
 - ³ J.-X. Yin, et. al., Quantum-limit Chern topological magnetism in $TbMn_6Sn_6$. *Nature* **583**, 533-536 (2020).
 - ⁴ Guguchia, Z. et al. Tunable anomalous Hall conductivity through volume-wise magnetic competition in a topological kagome magnet. *Nature Communications* **11**, 559 (2020).
 - ⁵ Nirmal J. Ghimire and Igor I. Mazin, Topology and correlations on the kagome lattice. *Nature Materials* **19**, 137-138 (2020).
 - ⁶ Ortiz, B. et al. CsV_3Sb_5 : A Z_2 Topological Kagome Metal with a Superconducting Ground State. *Phys. Rev. Lett.* **125**, 247002 (2020).
 - ⁷ Ortiz, B., Sarte, P., Kenney, E., Graf, M., Teicher, S., Seshadri, R., & Wilson, S. Superconductivity in the Z_2 kagome metal KV_3Sb_5 . *Phys. Rev. Materials* **5**, 034801 (2021).
 - ⁸ Yin, Q., Tu, Z., Gong, C., Fu, Y., Yan, S., & Lei, H. Superconductivity and normal-state properties of kagome metal RbV_3Sb_5 single crystals. *Chinese Phys. Lett.* **38**, 037403 (2021).
 - ⁹ Jiang, Y.-X. et al. Discovery of topological charge order in kagome superconductor KV_3Sb_5 . *Nature Materials* **20**, 1353-1357 (2021).
 - ¹⁰ Shumiya, N. et al. Tunable chiral charge order in kagome superconductor RbV_3Sb_5 . *Phys. Rev. B* **104**, 035131 (2021).
 - ¹¹ Wang, Z. et al. Electronic nature of chiral charge order in the kagome superconductor CsV_3Sb_5 . *Phys. Rev. B* **104**, 075148 (2021).
 - ¹² Mielke III, C. et al. Time-reversal symmetry-breaking charge order in a kagome superconductor. *Nature* **602**, 245-250 (2022).
 - ¹³ Guguchia, Z. et al. Tunable unconventional kagome superconductivity in charge ordered RbV_3Sb_5 and KV_3Sb_5 . *Nature Communications* **14**, 153 (2023).
 - ¹⁴ Khasanov, R. et al. Time-reversal symmetry broken by charge order in CsV_3Sb_5 . *Phys. Rev. Research* **4**, 023244 (2022).
 - ¹⁵ Yu, L. et al. Evidence of a hidden flux phase in the topological kagome metal CsV_3Sb_5 . arXiv:2107.10714 (2021).
 - ¹⁶ Xu, Y. et al. Three-state nematicity and magneto-optical Kerr effect in the charge density waves in kagome superconductors. *Nature Physics* **18**, 1470-1475 (2022).
 - ¹⁷ Hu, Y et al. Time-reversal symmetry breaking in charge density wave of CsV_3Sb_5 detected by polar Kerr effect, Preprint at <https://arxiv.org/abs/2208.08036>.
 - ¹⁸ Guo, C et al. Switchable chiral transport in charge-ordered kagome metal CsV_3Sb_5 . *Nature* **611**, 461-466 (2022).
 - ¹⁹ Neupert, T., Denner, M.M., Yin, J.-X., Thomale, R. and Hasan, M.Z.. Charge order and superconductivity in kagome materials. *Nature Physics* **18**, 137-143 (2022).
 - ²⁰ Yin, J.-X. Lian, B. and Hasan, M.Z. Topological kagome magnets and superconductors. *Nature* **612**, 647-657 (2022).
 - ²¹ S. Yang, et al., Giant, unconventional anomalous Hall effect in the metallic frustrated magnet candidate, KV_3Sb_5 . *Sci. Adv.* **6**, 1-7s (2020).
 - ²² Yu, F. et al. Concurrence of anomalous Hall effect and charge density wave in a superconducting topological kagome metal. *Phys. Rev. B* **104**, 041103 (2021).
 - ²³ Denner, M. Thomale, R. and Neupert, T. Analysis of charge order in the kagome metal AV_3Sb_5 ($A = K, Rb, Cs$). *Phys. Rev. Lett.* **127**, 217601 (2021).
 - ²⁴ Christensen, M.H., Birol, T., Andersen, B.M., & Fernandes, R.M. Theory of the charge-density wave in AV_3Sb_5 kagome metals. *Phys. Rev. B* **104**, 214513 (2021).
 - ²⁵ Park, T., Ye, M. & Balents, L. Electronic instabilities of kagome metals: Saddle points and Landau theory. *Phys. Rev. B* **104**, 035142 (2021).
 - ²⁶ Lin, Y.-P. & Nandkishore, R.M. Complex charge density waves at Van Hove singularity on hexagonal lattices: Haldane-model phase diagram and potential realization in the kagome metals AV_3Sb_5 . *Phys. Rev. B* **104**, 045122 (2021).
 - ²⁷ Song, D. et al. Orbital ordering and fluctuations in a kagome superconductor CsV_3Sb_5 . *Science China Physics, Mechanics and Astronomy* **65**, 247462 (2022).
 - ²⁸ Christensen, M.H., Birol, T., Andersen, B.M., & Fernandes, R.M. Loop currents in AV_3Sb_5 kagome metals: multipolar and toroidal magnetic orders. *Phys. Rev. B* **106**, 144504 (2022).
 - ²⁹ Pokharel, G. et al. Electronic properties of the topological kagome metals YV_6Sn_6 and GdV_6Sn_6 . *Phys. Rev. B* **104**, 235139 (2021).
 - ³⁰ Peng, S et al. Realizing Kagome Band Structure in Two-Dimensional Kagome Surface States of RV_6Sn_6 ($R=Gd, Ho$). *Phys. Rev. Lett.* **127**, 266401 (2021).
 - ³¹ Hu, Y. et al. Tunable topological Dirac surface states and van Hove singularities in kagome metal GdV_6Sn_6 . *Sci. Adv.* **8**, eadd2024 (2022).
 - ³² Suriya Arachchige, H.W. et al. Charge density wave in kagome lattice intermetallic ScV_6Sn_6 . *Physical Review Letters* **129**, 216402 (2022).
 - ³³ Hu, Tianchen et al. Optical spectroscopy and band structure calculations of structural phase transition in the Vanadium-based kagome metal ScV_6Sn_6 . Preprint at arXiv:2211.03412 (2023).
 - ³⁴ Manuel, T et al. Dynamics and Resilience of the Charge Density Wave in a bilayer kagome metal. Preprint at arXiv:2302.10699 (2023).
 - ³⁵ Yong, H. et al. Phonon promoted charge density wave in topological kagome metal ScV_6Sn_6 . Preprint at arXiv:2023.01.01 (2023).
 - ³⁶ Cheng, S et al. Nanoscale visualization and spectral fingerprints of the charge order in ScV_6Sn_6 distinct from other kagome metals. Preprint at arXiv:2302.12227 (2023).
 - ³⁷ Zhang, X et al. Destabilization of the Charge Density Wave and the Absence of Superconductivity in ScV_6Sn_6 under High Pressures up to 11 GPa. *Materials* **15**, 7372 (2022).
 - ³⁸ Dolomanov, O.V. et al. OLEX2: a complete structure so-

- lution, refinement and analysis program. *J. Appl. Cryst.* **42**, 339-341 (2009).
- ³⁹ Sheldrick, G.M. Crystal structure refinement with SHELXL. *Acta Cryst.* **C71**, 3-8 (2015).
- ⁴⁰ Momma, K. and Izumi, F. VESTA3 for three-dimensional visualization of crystal, volumetric and morphology data. *J. Appl. Cryst.* **44**, 1272/1276 (2011).
- ⁴¹ Giraldo-Gallo, P. et al. Scale-invariant magnetoresistance in a cuprate superconductor. *Science* **361**, 479-481 (2018).
- ⁴² M. Novak, S. Sasaki, K. Segawa and Y. Ando. Large linear magnetoresistance in the Dirac semimetal TlBiSSe. *Phys. Rev. B* **91**, 041203(R) (2015).
- ⁴³ Wei, X. et al. Linear nonsaturating magnetoresistance in kagome superconductor CsV₃Sb₅ thin flakes. Preprint at arXiv:2210.16890 (2022).
- ⁴⁴ Kubo, R. & Toyabe, T. Magnetic Resonance and Relaxation *North Holland*, Amsterdam, (1967).
- ⁴⁵ Huang, W. et al. Precision search for magnetic order in the pseudogap regime of La_{2-x}Sr_xCuO₄ by muon spin relaxation. *Phys. Rev. B* **85**, 104527 (2012).
- ⁴⁶ Luke, G.M. et al. Time-reversal symmetry breaking superconductivity in Sr₂RuO₄. *Nature* **394**, 559 (1998).
- ⁴⁷ Singh, A.D. et al. Time-reversal symmetry breaking and multigap superconductivity in the noncentrosymmetric superconductor La₇Ni₃. *Phys. Rev. B* **103**, 174502 (2021).
- ⁴⁸ Sedlak, K., Scheuermann, R., Stoykov, A., Amato, A. GEANT4 simulation and optimisation of the high-field μ SR spectrometer. *Physica B* **404**, 970-973 (2009).
- ⁴⁹ Yaouanc, A. & Dalmas de Reotier, P. Muon Spin Rotation, Relaxation, and Resonance: Applications to Condensed Matter. Oxford University Press (2011).
- ⁵⁰ Haldane, F.D.M. Model for a quantum Hall effect without Landau levels: condensed-matter realization of the parity anomaly. *Phys. Rev. Lett.* **61**, 2015-2018 (1988).
- ⁵¹ Varma, C.M. Non-Fermi-liquid states and pairing instability of a general model of copper oxide metals. *Phys. Rev. B* **55**, 14554-14580 (1997).
- ⁵² Canfield, P.C. Kong, T. Kaluarachchi, U.S. and Jo, N.H. Use of frit-disc crucibles for routine and exploratory solution growth of single crystalline samples. *Philos. Mag.* **96**, 84-92 (2016).
- ⁵³ Sheldrick, G.M. SHELXT - Integrated space-group and crystal-structure determination. *Acta Cryst.* **A71**, 3-8 (2015).
- ⁵⁴ Suter, A. and Wojek, B.M. Musfit: A Free Platform-Independent Framework for μ SR Data Analysis. *Physics Procedia* **30**, 69 (2012).

I. METHODS

Sample preparation: Single crystals of ScV₆Sn₆ were grown by the molten Sn flux method. The starting materials were Sc (3N, Alfa Aesar), V (2N8, Alfa Aesar), and Sn (99.9999 %, Alfa Aesar). In a helium-filled glovebox, Sc (0.218 g, 0.485 mmol), V (1.481 g, 2.908 mmol), and Sn (33.390 g, 28.127 mmol) were placed into a 5 ml alumina Canfield crucible⁵². The crucible set was placed into a quartz u-tube, evacuated, backfilled with c.a. 100 mbar of Ar, and sealed as an ampoule. The specimen was heated up to 1150 °C, with a rate of 400 °C/h, and annealed at that temperature for 12 h. Subsequently, the sample was cooled down to 780 °C with a rate of 100 °C/h. After the growth step, the excess Sn flux was separated from the single crystals by centrifugation.

Crystallography: A single crystal of ScV₆Sn₆, obtained from Sn flux, was mounted on the *MiTeGen MicroMounts* loop and used for a X-ray structure determination. Measurements were performed at RT on a *STOE STADIVARI* diffractometer equipped with a *Dectris EIGER 1M 2R CdTe* detector and with an *Anton Paar Primux 50 Ag/Mo* dual-source using Ag K_{α} radiation ($\lambda = 0.56083 \text{ \AA}$) from a micro-focus X-ray source and coupled with an *Oxford Instruments Cryostream 800* jet. The unit cell constants and an orientation matrix for data collection were obtained from a least-squares refinement of the setting angles of 16647 reflections in the range $6.7^{\circ} < 2\theta < 66.6^{\circ}$. A total of 3448 frames were collected using ω scans, 5 seconds exposure time and a rotation angle of 0.5° per frame, and a crystal-to-detector distance of 60.0 mm.

Data reduction was performed with *X-Area* package [*X-Area* package, Version 2.1, STOE and Cie GmbH, Darmstadt, Germany, 2022]. The intensities were corrected for Lorentz and polarization effects, and an empirical absorption correction using spherical harmonics was applied [*X-Area* package, Version 2.1, STOE and Cie GmbH, Darmstadt, Germany, 2022]. The structure was solved using *ShelXT*⁵³ and *Olexs*² program³⁸. The model was refined with *ShelXL* package³⁹ and *Olexs*² software.

Heat Capacity: Heat Capacity (C_p) measurements were performed in a Physical Properties Measurement System (PPMS, 14T, Quantum Design) at zero magnetic field using the relaxation method between 1.85 and 200 K. 7.75 mg of ScV₆Sn₆ crystal was fixed with the Apiezon-N grease to the sapphire holder of the calorimeter. The samples were then cooled down to 1.85 K, and the heat capacity measured by heating. The signal from the Apiezon-N grease and the calorimeter, previously measured under the same conditions, was subtracted from the data to obtain the sample's C_p .

Magnetotransport: Magnetoresistance of the single-crystal ScV₆Sn₆ was measured in physical property measurement system (PPMS-9, Quantum Design) using the typical four-probe technique. Four Pt-wires (0.0254 mm diameter) were attached by silver epoxy on the single crystal, polished into bar-shaped specimen. Electrical current of 1 mA and magnetic field was applied along

the crystallographic a - and c -axis, respectively, that were confirmed by Laue measurement.

μ SR experiment: In a μ SR experiment nearly 100 % spin-polarized muons μ^+ are implanted into the sample one at a time. The positively charged μ^+ thermalize at interstitial lattice sites, where they act as magnetic microprobes. In a magnetic material the muon spin precesses in the local field B_μ at the muon site with the Larmor frequency $\nu_\mu = \gamma_\mu/(2\pi)B_\mu$ (muon gyromagnetic ratio $\gamma_\mu/(2\pi) = 135.5 \text{ MHz T}^{-1}$).

Zero field (ZF) and transverse field (TF) μ SR experiments on the single crystalline sample of ScV_6Sn_6 were performed on the GPS instrument and high-field HAL-9500 instrument, equipped with BlueFors vacuum-loaded cryogen-free dilution refrigerator (DR), at the Swiss Muon Source (S μ S) at the Paul Scherrer Institut, in Villigen, Switzerland. A mosaic of several crystals stacked on top of each other was used for these measurements. The magnetic field was applied along the crystallographic c -axis. A schematic overview of the experimental setup for zero-field is shown in Figure 4a. The crystal was mounted such that the c -axis of it is parallel to the muon beam. Using the "spin rotator" at the π M3 beamline, muon spin was rotated (from its natural orientation, which is antiparallel to the momentum of the muon) by $44.5(3)^\circ$ degrees with respect to the c -axis of the crystal. So, the sample orientation is fixed but the muon spin was rotated. The rotation angle can be precisely estimated to be $44.5(3)^\circ$ by measurements in weak magnetic field, applied

transverse to the muon spin polarization. Zero field and high transverse field μ SR data analysis on single crystals of ScV_6Sn_6 were performed using both the so-called asymmetry and single-histogram modes^{49,54}. The experimental data were analyzed using the MUSRFIT package⁵⁴.

Competing interests: All authors declare that they have no competing interests.

Data Availability: All relevant data are available from the authors. Alternatively, the data can be accessed through the data base at the following link <http://musruser.psi.ch/cgi-bin/SearchDB.cgi>.

II. ACKNOWLEDGMENTS

The μ SR experiments were carried out at the Swiss Muon Source (S μ S) Paul Scherrer Institute, Villigen, Switzerland. Z.G. acknowledges support from the Swiss National Science Foundation (SNSF) through SNSF Starting Grant (No. TMSGI2_211750). Z.G. acknowledges the useful discussions with Robert Scheuermann. Y.H. and M.S. acknowledges support from the Swiss National Science Foundation under Grant. No. 200021_188413.